Applied Thermal Engineering 300 (2026) 131403

Contents lists available at ScienceDirect

Applied Thermal Engineering

journal homepage: www.elsevier.com/locate/ate

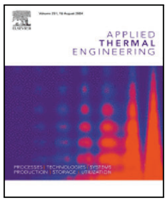

Research Paper

Temperature and densification nonuniformity during ultrafast high-temperature sintering

Andrew Caratenuto [*], David R. Clarke

School of Engineering and Applied Sciences, Harvard University, 150 Western Avenue, Boston, MA, 02134, USA

ARTICLE INFO

Keywords:
UHS
High-temperature materials
Sintering
Radiative heat transfer

ABSTRACT

Ultrafast high-temperature sintering (UHS) has recently been demonstrated for the rapid densification of materials. Its high heating rates (10^4 °C min^{-1}) and temperature capabilities (up to 3000 °C) enable rapid densification and high synthesis throughput with low volatilization. However, temperature nonuniformities may arise that can result in undesirable density inhomogeneities. To quantify, assess, and address these issues, we present a simulation model for coupled multimode heat transfer and concurrent densification kinetics. Thermal diffusion and radiative heat transfer are considered, and densification is modeled using a master sintering curve approach. Using simulated cases, the magnitudes and time scales of temperature and densification nonuniformities, coupled with the thermal and optical properties, are identified. We find that while the thermal properties of the material are important, the optical properties of the material can play a dominant role in the sintering dynamics, particularly at early stages. A new method of combining thermal, radiative, and optical properties to generalize the sintering kinetics is proposed, enabling rapid estimation of temperature nonuniformities and heating time scales for a given material and set of UHS parameters. Experimental validation is demonstrated by comparison with the sintering and densification alumina powder compacts. This confirms the accuracy of the model and illustrates its utility towards achieving uniform, dense materials by optimizing the UHS parameters through modeling.

1. Introduction

Manufacturing components by sintering powders typically involves making a shaped, pressed compact of individual powders and heating to high temperatures during which the compact densifies under the influence of various diffusion mechanisms [1–3]. Although sintering is a traditional manufacturing process that dates back to antiquity, it is also widely used to make a vast array of components critical to many industries such as electronics, energy generation and storage, and high-temperature applications [4–6]. The overall driving force for sintering is a reduction in the total surface and interface energy resulting in a reduction in the pore volume to form a dense, polycrystalline solid [5,7,8]. The various densification mechanisms are all thermally activated, albeit with different activation energies, so the kinetics are very dependent upon temperature. Conventional sintering can require many hours of heating the powder compact, holding at high temperatures for densification to occur followed by subsequent cooling. Consequently, it is an energy intensive process with low product and R&D throughput and high concomitant carbon emissions [7,9]. Complete densification by sintering is usually required as many physical properties, such as hardness, creep resistance, thermal conductivity and optical transparency are maximized at full density. Furthermore, a short time at very high temperatures minimizes grain growth and coarsening, permitting the densification of nanometer powders and the retention of sub-micron grain size essential for maximizing strength, hardness, optical transparency, and thermoelectric figure-of-merit, for instance.

Over the years, various rapid sintering techniques have emerged as potentially low-cost alternatives, such as fast firing, microwave sintering, and spark plasma sintering [7,10–12]. More recently, ultrafast high-temperature sintering (UHS) has been demonstrated [9] enabling densification within a few minutes or less. This technique uses Joule heating to quickly raise the temperature of conductive carbon heating elements ($\sim 10^4$ °C min^{-1}), providing rapid thermal radiative heating. Although particularly valuable for materials with high melting points, such as ceramics, UHS also shows promise for glasses, alloys, coating-substrate systems, and by minimizing losses of volatile elements [13–16]. The high heating rate has also been reported to enhance densification through numerous mechanisms, such as by reducing time spent in non-densifying sintering regimes and enabling non-equilibrium grain boundaries to raise the driving force of sintering [1–3,7,17].

---

[*] Corresponding author.
E-mail address: acaratenuto@seas.harvard.edu (A. Caratenuto).

https://doi.org/10.1016/j.applthermaleng.2026.131403
Received 18 December 2025; Received in revised form 31 March 2026; Accepted 8 May 2026

Nomenclature

Latin symbols

A	Area [m^2]
c_p	Specific heat capacity [J kg^{-1} K^{-1}]
D	Thermal diffusivity [m^2 s^{-1}]
d	Pore diameter [m]
d_{particle}	Particle diameter [m]
G	Incident radiation [W m^{-2}]
I	Radiation intensity [W m^{-2} sr^{-1}]
I_b	Blackbody radiation intensity [W m^{-2} sr^{-1}]
k	Intrinsic thermal conductivity [W m^{-1} K^{-1}]
k_{eff}	Effective thermal conductivity [W m^{-1} K^{-1}]
L	Sample thickness [m]
l	Absorption length [m]
n	Refractive index [–]
n_λ	Wavelength-dependent refractive index [–]
p	Dimensionless fitting parameter [–]
Q	Apparent activation energy [J mol^{-1}]
q_r	Radiative heat flux [W m^{-2}]
R	Ideal gas constant [J mol^{-1} K^{-1}]
r_s, r_p	Fresnel reflection coefficients [–]
R_{ext}	External hemispherical reflectance [–]
R_{int}	Internal hemispherical reflectance [–]
T	Temperature [K]
t	Time [s]
T_h	Heater temperature [K]
t_{ss}	Time to steady state [s]
x	Spatial coordinate [m]

Greek symbols

α	Absorption coefficient [m^{-1}]
α_{dense}	Absorption coefficient of dense solid [m^{-1}]
ΔT	Surface–center temperature difference [K]
ΔT_{max}	Maximum temperature difference [K]
Δx	Element thickness [m]
κ	Extinction coefficient (imaginary refractive index) [–]
λ	Wavelength [μm]
μ	Direction cosine [–]
ω	Scattering albedo, $\sigma_s/(\sigma_s+\alpha)$ [–]
ϕ	Porosity [–]
Ψ	Optical proportionality function [–]
ρ	Density [kg m^{-3}]
ρ_{rel}	Relative density [–]
σ	Stefan–Boltzmann constant [W m^{-2} K^{-4}]
σ_s	Scattering coefficient [m^{-1}]
Θ	Sintering function (MSC) [–]
ε_h	Heater emittance [–]

Despite its promise, temperature and sintering nonuniformities can limit the use of UHS [7]. When current is applied, volumetric Joule heating very rapidly raises the temperature of the carbon heating elements. In contrast to traditional sintering practice, the temperature of the material being sintered will not increase as quickly as that of the heater, especially in the early stages. The heater transfers energy to the material primarily through radiation, most of which is emitted between wavelengths of 1 to 10 μm [18] since carbon has a near-unity emittance at the relevant temperatures. Depending on the optical and thermal properties of the material, it may experience high temperature nonuniformity through the thickness of the part. Furthermore, since the thermal mass of the body is typically greater than that of the heating elements as well, there will inevitably be a delay in the thermal response. Highly absorbing materials absorb radiation primarily at the surface, inducing a rapid near-surface temperature rise; by contrast, weakly absorbing materials heat more slowly but with greater depth uniformity. Once absorbed, energy is transferred through the material by conduction and radiation with a strong dependence on thermal and optical properties.

Temperature nonuniformities are undesirable, as they can introduce densification (and hence stress) gradients. These can, in turn, limit densification due to constrained sintering and, in severe cases, cause crack formation [11,19,20]. In contrast, an uncertain thermal history may result in underheating or overheating, respectively, yielding insufficient densification or excessive grain growth [8,21,22]. These problems are exacerbated by the accelerated time scales of sintering in UHS, enhancing temporal sensitivity [7,17].

Without an accurate thermal history of the material, suitable UHS procedures can only be designed ad hoc. This is both time- and resource-intensive and may not deliver fully optimized results due to limited testing granularity. Sample temperatures may be pre-calibrated with respect to heater temperatures, as has been employed by Guo and Todd [17], but these methods do not provide any information on temperature gradients. The calibrations must be performed with a calibrant of identical composition and size to the material of interest and require continuous temperature measurement (e.g., with a thermocouple) during representative UHS processes. This can provide a more reliable measure of thermal response within the body. Yet, besides the considerable experimental effort required for accurate calibration results, it cannot account for material property changes during sintering, is unlikely to provide a measure of temperature uniformity within the body, and requires the pre-creation of a dense and uniform sintered body (which may not be feasible without calibration information). To the best of our knowledge, a detailed analysis of UHS thermal transport behaviors that considers material variations and densification has not been reported. Simultaneously, efficient progress in UHS materials synthesis requires a more accurate, less resource-intensive, and more generalizable approach to optimize sintering processes.

To aid in the development of the UHS process, we present a comprehensive analysis of the influence of material choice, geometry, and sintering parameters on temperature and densification uniformity during UHS. To this end, have constructed a model that simulates temperature distributions and densification during UHS, both temporally and spatially, by combining the energy and radiative transfer equations with an empirical relation for sintering densification, represented by the master sintering curve (MSC) approach [23]. We consider the effects of conduction, radiation and densification to accurately model heat transfer and sintering simultaneously. Nonlinear dependencies in thermal and optical properties incorporate the effects of density, temperature, and microstructure throughout the simulation. After describing the model, we present results that identify the properties most influential to thermal response and estimate thermal nonuniformities for a variety of process and material parameters. Then, we identify how integrating densification using MSCs influences transient thermal behaviors. Finally, to provide an experimental validation, we sinter alumina (aluminum oxide) powders using UHS under a variety of conditions and compare the findings with the model. Good agreement between experimental and modeled density is found, and parameters which can be optimized to achieve dense and uniform sintered materials are identified. These results and the simulation model will facilitate uniform, dense, and more reproducible UHS products with significantly reduced experimentation.

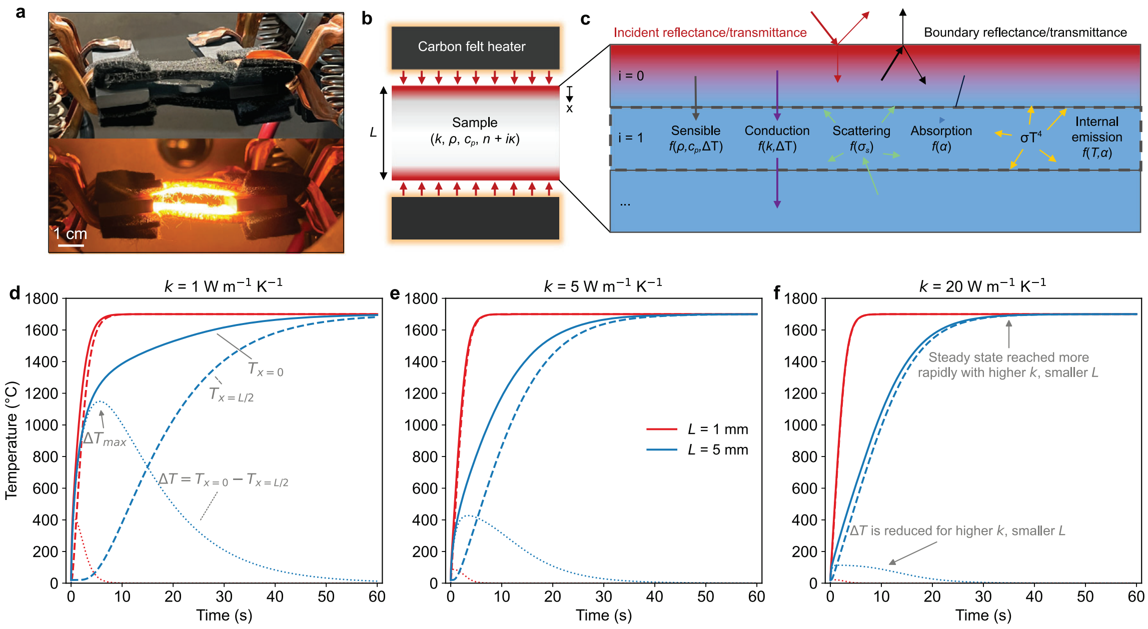

Fig. 1. UHS system and model overview. (a) Images of in-house UHS system, showing ceramic sample sandwiched between two carbon felt heaters. (b) Schematic representation of sample as modeled. (c) Expanded detail of energy transfer mechanisms modeled within the sample. (d–f) Temperature versus time curves for a highly absorbing medium undergoing UHS at 1700 °C. Several thermal conductivity and thickness values are considered. Solid lines show the top surface temperature, dashed lines show the midpoint temperature, and dotted lines show the temperature difference ΔT between the surface and center (the largest temperature difference within the medium due to symmetry). Note that k refers to the intrinsic thermal conductivity of the sample material, rather than the bulk thermal conductivity k_{eff}, which accounts for porosity.

2. Model

2.1. Modeled system and governing equations

To fabricate bulk materials by UHS, compacted powder samples are placed between two carbon felt heaters, one above and one below. A high-current electrical power supply is connected to the heaters to provide Joule heating (Fig. 1a). The sample thickness is typically small with respect to its lateral extent (e.g., thin discs) [9]. This high aspect ratio facilitates modeling a material as a 1D medium heated symmetrically from the top and bottom, as shown schematically in Fig. 1b–c ("medium" is used to refer to an arbitrary material simulated in this model). In 1D, the energy balance in this medium is [18,24]:

$$\rho c_p \frac{\partial T}{\partial t} = \frac{\partial}{\partial x}\left(k_{\text{eff}} \frac{\partial T}{\partial x}\right) - \frac{\partial q_r}{\partial x}, \tag{1}$$

where ρ and c_p are the density and specific heat of the medium, respectively, T is temperature, x is the depth, and t is time. This equation uses the effective thermal conductivity of the bulk sample, k_{eff}, which is a function of both the intrinsic thermal conductivity k of the material as well as the porosity of the medium. The energy balance is coupled to radiative transfer through divergence of the radiative heat flux q_r. This consideration of radiative transfer within the sample, as opposed to modeling only conduction with radiative boundary conditions, is essential to energy transport in UHS. When samples are not highly absorbing and non-scattering, solutions deviate greatly from a corresponding conduction-only case, as will be illustrated later.

Samples are considered to have absorptive, emissive, and scattering properties. They are also assumed to be "gray" bodies, meaning that their optical properties (refractive index, scattering coefficient, and absorption coefficient) are independent of wavelength. For this case, the radiative flux divergence is given by [18]:

$$\frac{\partial q_r}{\partial x} = (1-\omega)(\alpha + \sigma_s)(G - I_b). \tag{2}$$

Here, α and σ_s are the absorption and scattering coefficients of the medium, respectively, and the scattering albedo ω is given by $\omega = \sigma_s/(\sigma_s + \alpha)$. The emitted thermal radiation intensity I_b is obtained from $I_b = n^2\sigma T^4/\pi$, where n is the refractive index of the medium and σ is the Stefan–Boltzmann constant. The sum of incident radiation G is calculated based on the intensity (I) distribution, which is obtained from the radiative transfer equation (RTE):

$$\mu \frac{\partial I}{\partial x} = -(\alpha + \sigma_s)I + \frac{\sigma_s}{4\pi}\int_{4\pi} I \, d\Omega' + \alpha I_b, \tag{3}$$

where μ is the direction cosine for each direction Ω. Hence, the energy balance and RTE are coupled through T and q_r, and may be discretized and solved iteratively for convergence.

2.2. Boundary conditions and assumptions

Solution of both the energy and radiative transfer equations require boundary conditions at the top and bottom surfaces. In practice, samples are typically in close contact with the heater on one or both sides during the UHS process. The carbon heaters are often felts, so there is only occasional point contact between the heater and the powder compact. Consequently, conductive and convective heat fluxes at the boundary surfaces are considered negligible relative to the radiative fluxes (justification for this assumption is given in the supplementary text). Thus, the energy equation is given a zero flux condition ($\partial T/\partial x = 0$) at both boundaries, corresponding to negligible conduction and convection at these surfaces. Heat transfer in and out of the medium is assumed to take place solely by radiation, which is accounted for in the radiative flux divergence term. Taking into account surface reflection, the boundary conditions for forward-moving and backward-moving radiation at the top ($x = 0$) and bottom ($x = L$) boundaries are, respectively:

$$I_{+,x=0} = R_{\text{int}} I_- + \left(1 - R_{\text{ext}}\right) \frac{\sigma}{\pi} \varepsilon_h T_h^4 \tag{4}$$

and

$$I_{-,x=L} = R_{\text{int}} I_+ + \left(1 - R_{\text{ext}}\right) \frac{\sigma}{\pi} \varepsilon_h T_h^4. \tag{5}$$

Here, T_h and ε_h are the temperature and emittance of the heaters, and R_{ext} and R_{int} are the external (incoming) and internal (outgoing) surface reflectances, respectively. Though this problem is typically symmetric, we generalize the approach for separate boundary conditions to enable simple extension to non-symmetric cases (e.g., one-sided heating of a coating on a substrate). From a radiative perspective, the heater-medium interfaces are considered to be separated by a thin layer of inert gas (or vacuum) and the surfaces are microscopically rough. Due to the strong scattering of thermal radiation by compacted powders, a hemispherical approximation for Fresnel reflectance is utilized. The hemispherical reflectance for incoming radiation is obtained by multiplying the s and p reflectance coefficient arithmetic means by the direction cosine μ and integrating over all angles [18]:

$$R_{\text{ext}} = 2\int_0^1 \frac{1}{2}\left(|r_s|^2 + |r_p|^2\right)\mu\, d\mu. \tag{6}$$

The corresponding hemispherical reflectance for outgoing radiation can be obtained from [25]:

$$R_{\text{int}} = 1 - \frac{1}{n^2}(1 - R_{\text{ext}}). \tag{7}$$

Finally, isotropic scattering is assumed.

2.3. Thermal, optical and domain properties

Powder compacts experience rapid changes in temperature and density during UHS. Many of the thermal, optical and material properties which govern energy transfer are dependent upon temperature and density, both of which may be nonuniform within the domain. As such, it is essential to model how thermal and optical properties change with temperature, density, location, and time within the medium, and to achieve convergence of these properties with the temperature and density solutions at each timestep.

Densification is modeled according to the master sintering curve (MSC) approach, originally introduced by Su and Johnson [23]. In the absence of other models, this is an empirical method that has been widely adopted in the ceramics and powder metallurgy literature to describe densification. It uses densification data, obtained through a set of varied sintering experiments on a given material, to model the densification of the material for any temperature schedule. Construction of an MSC requires fitting experimental relative density data (ρ_{rel}, defined as the ratio of the bulk density to the theoretical density) to a sintering function Θ, defined by Su and Johnson as [23]:

$$\Theta(t, T(t)) = \int_0^t \frac{1}{T}\exp(-\frac{Q}{RT})dt. \tag{8}$$

Θ is readily calculated from the temperature history of the material and a material-specific fitting parameter Q, defined as the apparent activation energy of sintering. Crucially, this definition of Θ makes ρ_{rel} independent of heating rate. Thus, with an established MSC of a material (including Q), Θ may be calculated from the temperature history, and ρ_{rel} may be determined.

In our model, Θ is evaluated at each spatial coordinate and timestep based on the thermal history up to that time. The relative density is then obtained by interpolating the MSC. One of the characteristic features of sintering is that samples shrink due to densification. To account for this, and to satisfy mass conservation, a Lagrangian frame of reference is used to keep the mass constant within a given computational cell. According to the 1D slab assumption, the element thickness Δx at location i shrinks as the material densifies according to $\Delta x_i^{(m+1)} = \Delta x_i^{(m)}\rho^{(m)}/\rho^{(m+1)}$, where m represents the time step. This treatment preserves mass while simulating densification.

It is worth noting that the MSC approach is designed for isothermal heating at different times and temperatures where one sintering mechanism dominates [23], which may not be satisfied during UHS because of the rapid increases in temperature. Recent literature suggests that the MSC approach is suitable for predicting UHS densification, but that UHS may accelerate sintering due to non-equilibrium grain boundaries requiring a slight adaptation of the MSC approach [17]. Therefore, while an unmodified MSC may not fully capture the sintering dynamics of some cases, this approach still simulates the dynamics and interdependencies of energy transfer during UHS, and provides, as will be shown later, accurate predictions of densification. We also note that the MSC is an empirical model, which does not include the constitutive equations required to simulate the full elastic and visco-elastic thermomechanics of sintering. Thus, stress and strain are not considered explicitly here. Nonetheless, temperature and/or densification nonuniformities are appropriate indicators of the possibility of constrained sintering, which is of primary interest for enhancing the viability of UHS.

Thermal conductivity k and specific heat c_p are generally temperature dependent (at least up until high temperatures), and tabulated temperature-dependent data can be readily incorporated into this model. However, k_{eff} is a function of both k and ρ_{rel}. A green or partially sintered material can be considered a mixture of a fluid (e.g., inert gas or vacuum) and a solid. The effective thermal conductivity of porous or composite materials is highly dependent on morphology and connectivity [26]. Detailed models have been constructed for many limiting cases, and discussion of model appropriateness and accuracy continues in the literature [27–29]. As this work is concerned with establishing general trends of temperature and densification during UHS, we choose a simple first-order approximation for k_{eff} for the case of low-conductivity spherical pores ($k_{\text{eff}} = k\left(1 - \frac{3}{2}\phi\right)$, where ϕ is the porosity). This formulation is applicable to green and partially sintered bodies used in UHS, and captures the increase in effective thermal conductivity that accompanies densification.

Variations of optical properties with respect to both relative density and wavelength are considered in our model. We choose to neglect the influence of temperature on optical properties; while refractive indices can exhibit temperature dependence, the magnitude of these changes is generally small (especially for common ceramics) [30]. Densification will, however, modify both the absorption and scattering coefficients. The absorption coefficient α of a material is given by $4\pi\kappa/\lambda$, where κ and λ are the extinction coefficient and wavelength, respectively (note that "extinction coefficient" here refers to the imaginary portion of the complex refractive index, and not the sum of the absorption and scattering coefficients as is used in some contexts [25]). However, this definition for α pertains to a fully dense material. Pores have negligible absorption, so α must be scaled to account for the reduced solid volume of a porous material. Therefore, the absorption coefficient of the porous medium is scaled with relative density according to $\alpha = \alpha_{\text{dense}}\rho_{\text{rel}}$, where α_{dense} is the absorption coefficient of the fully dense solid.

As powder compacts often consist of individual powder particles of comparable length scale to thermal emission wavelengths, optical scattering may be significant and scattering will influence the energy transfer during UHS [25]. We calculate scattering coefficients based on Mie theory using a pre-built Python package assuming spherical inclusions (inert gas or vacuum pores) [31]. To obtain accurate scattering efficiencies and coefficients from Mie theory, the size of the scattering object must be known. As powder compacts are most easily defined by the solid particle diameter, we use the Kozeny equation to obtain pore size from density and particle diameter,

$$d = \frac{2}{3}d_{\text{particle}}\left(\frac{1 - \rho_{\text{rel}}}{\rho_{\text{rel}}}\right), \tag{9}$$

which was reported to agree well with measured pore sizes for green compacts [32]. The evolution of pores during sintering is a complex process. The majority of pores shrink with densification during sintering, though some may also coalesce and grow in certain cases [33,34]. For generality, we assume that the number of pores in the medium remains the same as densification proceeds, and that all pores shrink uniformly with densification. Based on this scaling assumption, the new pore size is calculated at each time step based on ϕ as $d^{(m+1)} = d^{(m)}\left(\phi^{(m+1)}/\phi^{(m)}\right)^{1/3}$.

Using these strategies, the dependence of absorption and scattering coefficients on density are continually updated in the simulation. While it is assumed that the thermal radiation is gray, optical properties may vary within the range of relevant thermal wavelengths. To account for this, a gray approximation for wavelength-dependent optical properties is obtained based on a Planck average from 0.2–10 μm, covering the relevant thermal radiation wavelength range for most UHS temperatures. For example, the refractive index is calculated from wavelength-dependent data (n_λ) as:

$$n = \frac{\int_{0.2\ \mu\mathrm{m}}^{10\ \mu\mathrm{m}} n_\lambda(\lambda) I_{bb}(T_h,\lambda)\,d\lambda}{\int_{0.2\ \mu\mathrm{m}}^{10\ \mu\mathrm{m}} I_{bb}(T_h,\lambda)\,d\lambda}, \tag{10}$$

where I_{bb} is the Planck function for blackbody radiation [18]. The heater temperature T_h is used for this weighting scheme as this is most representative of the radiation incident on and propagating within the medium. Absorption and scattering coefficients are averaged using the same scheme. Thus, using the strategies discussed in this section, the model incorporates the dependencies of temperature, density, particle size, and wavelength on thermal transport and densification during the UHS process.

2.4. Implementation and solution method

Using the methods outlined above, a combined heat transfer and densification model is implemented in Python. The energy balance is discretized using an implicit scheme for stability. The RTE is solved by discretizing according to the discrete ordinates method (DOM), using backwards difference for forward-moving radiation and forward difference for backward-moving radiation. At each timestep, the RTE is first solved using a matrix formulation, providing a solution for the radiative flux divergence throughout the domain. These values are then used to solve the energy balance using a separate matrix formulation. The solver alternates between the RTE and energy balances until convergence is reached, proceeding to the next timestep thereafter.

The nonlinearity within this modeled scheme is large. In addition to the interdependence of the radiative transfer and energy equations, ρ, k, and c_p are functions of temperature, k_{eff}, α, σ_s and Δx are functions of ρ_{rel}, and changes to any property may modify the temperature distribution. To ensure reliability of the calculation results, we utilize robust solution convergence and discretization criteria. For temperature and other time varying properties, a convergence criterion of approximately 0.1% of their minimum value was applied. Time and space discretizations are chosen according to solution independence, where they are reduced until the solution becomes independent of their choice. This modeling framework is the basis for the simulation results presented in the following, with any deviations explicitly noted.

3. Model results

3.1. Thermal properties

A variety of simulation results are presented to understand the influence of different variables on the UHS process. First, the influences of thermal properties are isolated from radiative properties by considering a highly absorbing ($\alpha = 10^5$ m^{-1}) and non-scattering medium (this baseline case is analogous to transient conduction in a 1D slab with radiative boundary conditions). These initial analyses assume constant thermal and optical properties and a constant density of $\rho_{\mathrm{rel}} = 0.6$ (based on random packing of equal sized spheres). These simulations are performed using properties of alumina ($\rho = 4000$ kg m^{-3}, $c_p = 1250$ J kg^{-1} K^{-1}, $n = 1.71$) as a representative material undergoing UHS at 1700 °C for 60 s.

In Fig. 1d–f, temperature versus time curves are shown for samples of varying thickness and intrinsic thermal conductivity (note that varying k here is equivalent to varying k_{eff}, since ρ_{rel} is constant). Temperatures at the outer surface and center of the medium, as well as the temperature difference ΔT between these planes, are plotted. The temperature difference arises due to the high surface absorption of incident thermal radiation, resulting in rapid heating of the outer surface and constrained energy propagation to the inner layers. Increases in sample thickness and decreases in thermal conductivity result in larger values of ΔT, as expected. Thicker and less conductive samples also take longer to reach equilibrium because of their larger heat capacity and lower thermal diffusivity.

Several characteristic quantities are identifiable from the temperature versus time simulations. The first is the maximum value of ΔT that occurs in the early stages of UHS, which is critical to material uniformity. Large differences in temperature during sintering can lead to differential sintering; in the case of UHS, preferential heating at the surface can cause the surface to densify more rapidly than the center. Inhomogeneous densification can introduce a stress gradient in two or three dimensions which can limit overall density and cause additional issues such as fracture [11,19,20]. It is therefore of paramount importance to minimize $\Delta T_{\max}$, especially once densification begins. The second parameter of importance is the time required to reach steady state t_{ss}, defined as the time at which all temperatures in the medium have reached 99% of the heater temperature. Due to the rapid rates of densification in UHS, having a detailed understanding of the heating rates and temperatures within the sample is essential to produce dense, uniform materials. For example, excessive heating and time at temperature can cause undesirable effects such as grain coarsening [8,21,22], while insufficient sintering time will produce incomplete densification. For these reasons, we utilize $\Delta T_{\max}$ and t_{ss} as proxies to quantify nonuniformity produced during the UHS process. This enables parametrization and comparison of thermal response as functions of material properties and system configurations.

Accordingly, Fig. 2 presents $\Delta T_{\max}$ and t_{ss} as functions of thermal conductivity and thickness, with all other parameters kept constant with the values stated previously. As in the previous simulations, both a lower k and a larger L reduce temperature uniformity and extend the initial transient heating period. This follows from Fourier's law: for a constant heat flux input, ΔT is proportional to L and inversely proportional to k. In particular, $\Delta T_{\max}$ trends quite clearly with the conductive thermal resistance of the medium (L/k). Plotting the data of Fig. 2a against the conductive resistance (Fig. 2c), it becomes obvious that L/k, rather than the specific values of k and L, has a primary role in determining $\Delta T_{\max}$. A formal derivation of this relationship is provided in the supplementary text. Similarly, a lower k and larger L extend the time required to reach steady state. This is expected as a lower k reduces the thermal diffusivity D, and a larger L increases the total mass of the system and the distance over which energy must diffuse. To analyze this trend in more detail, we derive a scaling parameter for t_{ss} from the governing equations, as shown in the supplementary text. It is found that the steady state time is proportional to the sum of conductive and radiative heat transfer resistances, multiplied by the thermal mass: $L^2/4D + L\rho c_p/2\sigma T_h^3$. The basis for this is that energy must overcome both of these resistances, in series, for the volume in the center of the sample to equilibrate.

Fig. 2 illustrates the strong influence of L/k on $\Delta T_{\max}$ and of $L^2/4D + L\rho c_p/2\sigma T_h^3$ on t_{ss}, respectively. However, independent influences of ρ and c_p must also be considered. For this reason, simulations were performed with varying ρ and c_p. Values of n and T_h are kept the same as in previous cases, and k and L are given constant values of 5 W m^{-1} K^{-1} and 2.5 mm, respectively. The results (Fig. S4) indicate that $\Delta T_{\max}$ is insensitive to ρ and c_p, and that t_{ss} trends upwards with both larger ρ and larger c_p. The former behavior confirms that L/k is the dominant factor in determining $\Delta T_{\max}$ in highly absorbing materials. The latter trend is expected based on the dependence of t_{ss} on thermal

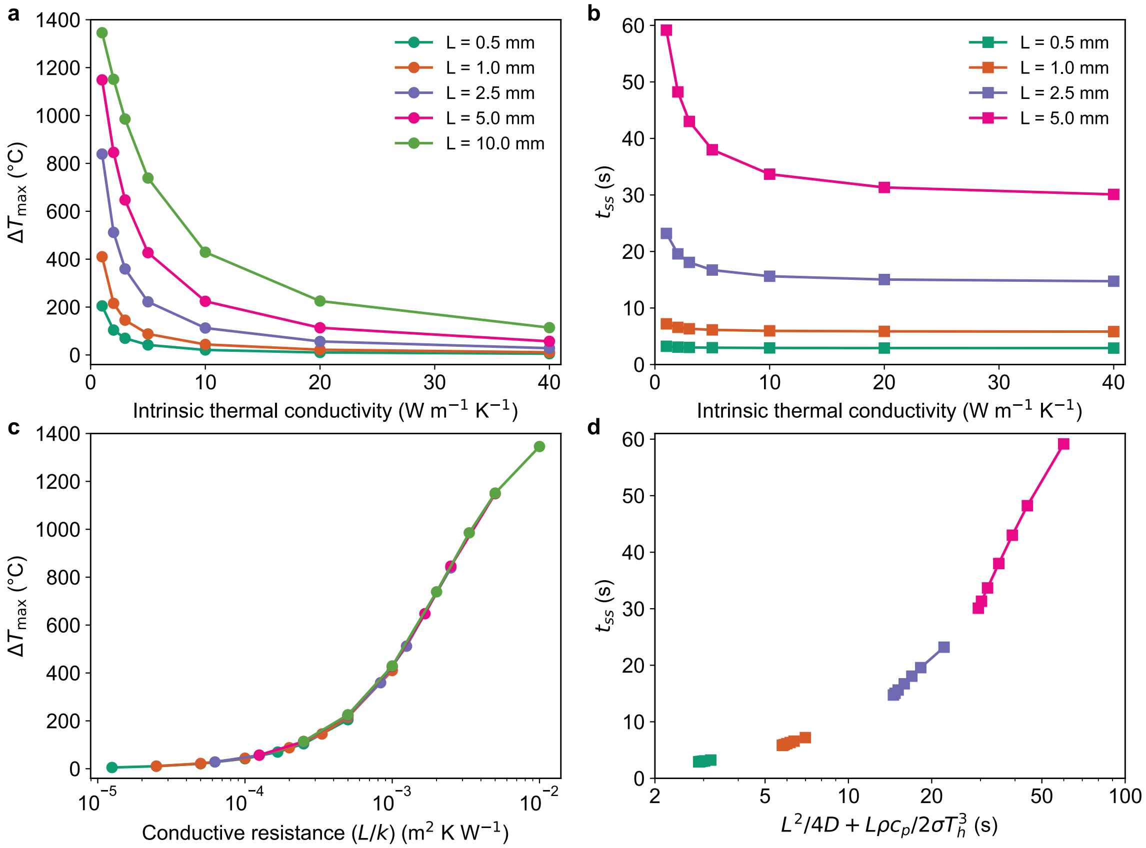

Fig. 2. Influence of thermal properties on heating trends in highly absorbing media. Effects of intrinsic thermal conductivity k and medium thickness L on (a) maximum temperature difference and (b) steady state time. (c–d) Same data as (a) and (b) plotted against the conductive resistance L/k and $L^2/4D{+}L\rho c_p/2\sigma T_h^3$, respectively.

mass elucidated earlier. Plotting both variables against the volumetric heat capacity $\rho \cdot c_p$ results in all data series collapsing to one curve, as seen in Fig. S4. This illustrates that ρ and c_p modify the thermal response only through their effect on the volumetric heat capacity, supporting the dependence of t_{ss} on $L^2/4D + L\rho c_p/2\sigma T_h^3$.

In addition to the dependence on the material properties, the UHS heater temperatures and heating rates will also influence the thermal response of a sample. In Fig. 3a–b, simulation results are presented for varying heater temperatures and thicknesses, with other constants retaining the same values noted earlier. The trends are unsurprising — $\Delta T_{\max}$ is proportional to T_h, and t_{ss} is inversely proportional to T_h. This is because higher heater temperatures produce larger incident heat fluxes, leading to sharper temperature differences but more rapid heating of the sample. As noted previously, limiting temperature nonuniformity is critical for a high material density and uniformity. One method to reduce $\Delta T_{\max}$ is to decrease the heating rate, as shown in Fig. 3c–d for a 2.5 mm thick medium. Doing so reduces $\Delta T_{\max}$ substantially – especially at higher sintering temperatures – as the sample has more time to equilibrate at lower temperatures. Practically, if uniformity and density are hindered by differential sintering and/or nonuniformity, the temperature setpoint may be approached more slowly to remedy this. The consequence of a slower ramp time (t_r) is a prolonged t_{ss}, as the time-integrated heat flux in the early stages of heating is reduced. In general, a prolonged t_{ss} can be detrimental to densification, as much of the benefit of UHS stems from rapidly reaching high temperatures. However, extending the ramp time only raises t_{ss} on the order of seconds or minutes, which remains far more rapid than the time scales of conventional sintering. Based on this result, prescribing a t_r of 60–90 s can be a simple yet effective option to enhance sintering uniformity for many materials.

To confirm the derived scaling parameters and provide a simple method for estimating $\Delta T_{\max}$ and t_{ss}, we plot the results of all previous parameterizations against these parameters in Fig. 4. This data encompasses wide variations in L, k, ρ, c_p, T_h, and ramp time t_r. To accommodate these additional variables, the scaling parameters are extended to include terms for T_h and t_r, as described in the supplementary text. The data is found to fit well with a power law for $\Delta T_{\max}$ and a simple linear model for t_{ss}, as shown in the fit equations given in each plot. Consequently, these equations may be used directly to estimate UHS temperature nonuniformity and heating time scale for opaque materials, providing a simple and rapid estimation for sintering process design.

3.2. Optical properties

The previous section has discussed thermal response trends in highly absorbing, non-scattering media. However, in the visible/infrared where UHS heating is dominant, many ceramics are translucent, powder compacts are often highly scattering, and n varies greatly for different material choices. Therefore, we now consider how variations in optical properties influence the thermal response, illustrated through the simulation results of Figs. 5–7. Unless otherwise stated, k = 5 W m^{-1} K^{-1}, c$_p$ = 1250 J kg^{-1} K^{-1}, ρ = 4000 kg m^{-3}, ρ_{rel} = 0.6, n = 1.71, T_h = 1700 °C (instantaneous ramp), and L = 2.5 mm. Where σ_s or scattering albedo ω are not explicitly specified (Figs. 5a–b), results are for non-scattering media.

First, the influence of complex refractive index $\bar{n}$ is studied in Figs. 5a–b. The real component n mainly influences two quantities: the Fresnel reflectance at the surface, which is proportional to n (as shown in Fig. 5c), and the internal emitted intensity I_b, which scales with n^2. A

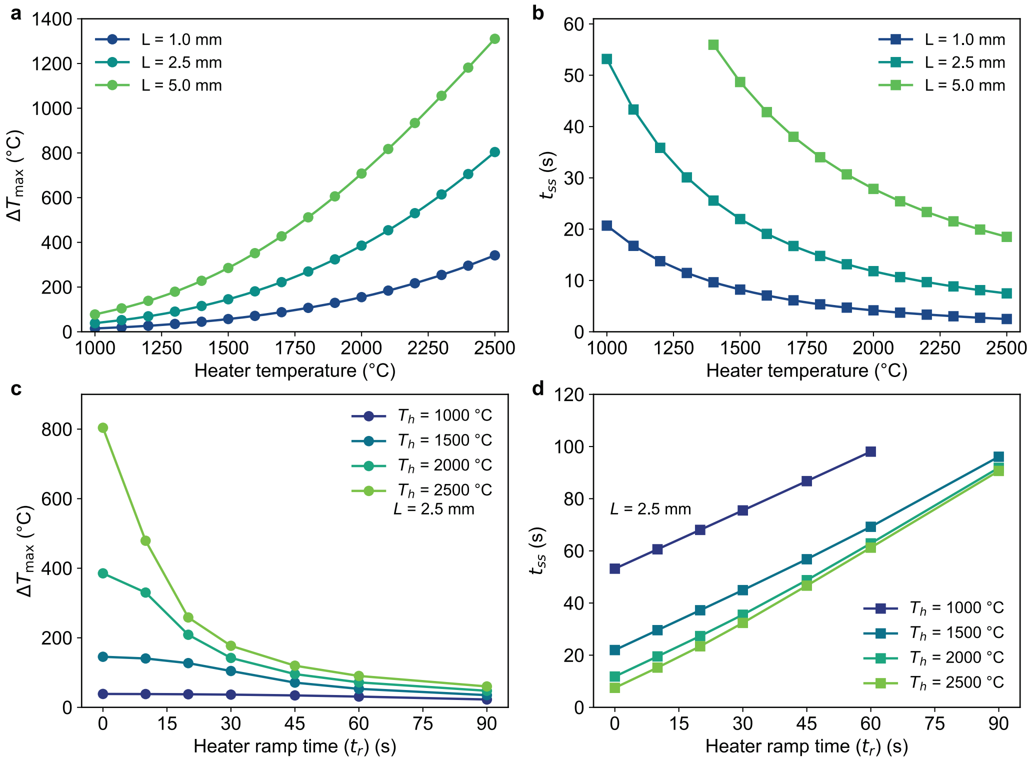

Fig. 3. Influence of UHS sintering parameters on thermal response in highly absorbing media. Effect of UHS heater temperature and thickness L on (a) maximum temperature difference and (b) steady state time. Effect of UHS heating rate and heater temperature (c) maximum temperature difference and (d) steady state time. Simulations in (b) and (d) are performed for simulation times of 60 s and 120 s, respectively. For cases which do not reach steady state within the simulation time, values are omitted from the plots.

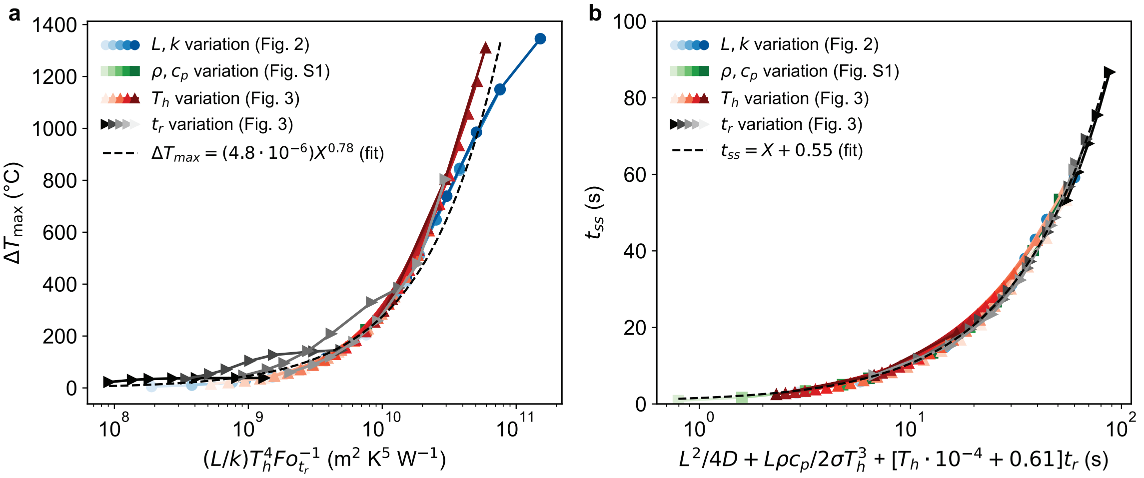

Fig. 4. Expanded scaling and best fit lines. Combined datasets for (a) $\Delta T_{\max}$ and (b) t_{ss}, plotted against their identified scaling parameters. For the line of best fit equations, $X = (L/k)T_h^4 Fo_{t_r}^{-1}$ for (a) and $X = L^2/4D + L\rho c_p/2\sigma T_h^3 + (T_h \cdot 10^{-4} + 0.61)t_r$ for (b).

higher reflectance reduces the incoming heat flux, thereby slowing the rate of temperature increase. In most regions, this effect dominates such that higher values of n yield lower values of $\Delta T_{\max}$ and higher values of t_{ss}. However, this trend is not independent of the imaginary component κ, which is directly proportional to the absorption coefficient. The absorption length l – equal to $1/\alpha$ – indicates the depth at which an intensity is attenuated by a factor of $1/e$ (i.e., reduced to 37% of its original value). Within $3l$, 95% of the intensity will have been absorbed. Therefore, when the medium thickness L is approximately $3l$, incident intensity is completely absorbed, but this absorption is distributed volumetrically rather than occurring at the surface. For L = 2.5 mm, this corresponds roughly to $\alpha = 10^3$ m^{-1}, shown as a dashed line in Figs. 5a–b. Above this threshold, absorption becomes more localized at the surface, while below this threshold, a portion of the incident radiation may transmit through the medium without being absorbed.

Correspondingly, an inflection point in the observed trends occurs at $L = 3l$. At lower values of α, t_{ss} rises sharply as a result of the incomplete absorption of incident radiation. Temperature differences approach zero, due to both a lower heat flux and a more uniform distribution of absorption. At higher values of α, $\Delta T_{\max}$ rises as absorption becomes increasingly localized at the surface. Once α reaches 10^5 m^{-1}, radiation is absorbed within the first few microns of the medium, typically in the range of the particle size. Further increases

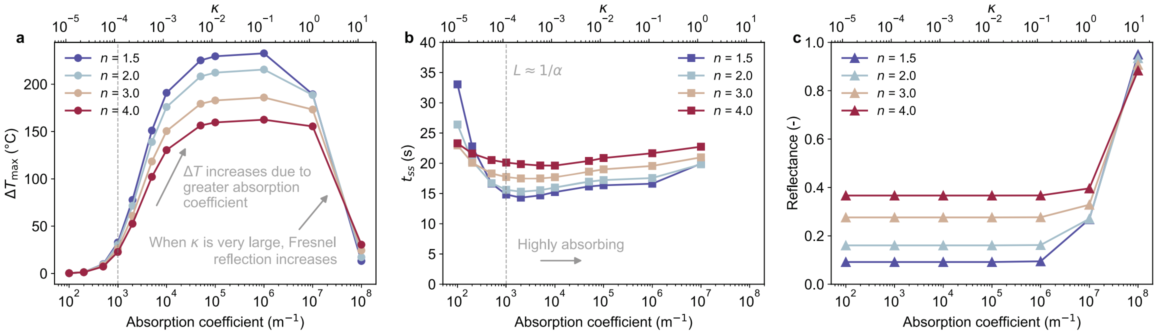

Fig. 5. Influence of optical properties on thermal response during UHS. Effects of refractive index and absorption coefficient on (a) maximum temperature difference and (b) steady state time. Time data for simulations which did not reach steady state within 60 s are omitted. Extinction coefficient values corresponding to each absorption coefficient are shown on the top x-axis. (c) Hemispherical Fresnel reflectance values for media of varying complex refractive indices.

in absorption have little influence, until κ reaches the same order of magnitude of n, at which point the Fresnel reflectance becomes very large (Fig. 5c). The effects of this are similar to the trends noted for higher n: a prolonged t_{ss} and a reduced ΔT_{max}, both due to a limited incident heat flux.

Note that when α is very small, a lower n extends t_{ss}. This appears counterintuitive, as a higher Fresnel reflectance generally prolongs heating as seen in the remainder of these curves. However, when α is sufficiently small, its magnitude is comparable to the n^2 term in I_b. Both n and α contribute to emission; hence, when they are of comparable magnitude, changes in n^2 have a noticeable influence on the strength of internal emission. Therefore, a higher n results in more efficient radiative transfer within the medium, reducing t_{ss} when α is small enough. Of additional note is the minimum in t_{ss} observed at $L = 3l$. At this point, the medium absorbs all incident energy from the heaters, but with maximum uniformity within the volume (as dictated by the Beer–Lambert law). This condition results in the most time-efficient heating of the medium while maintaining a low value of ΔT_{max}. In terms of sintering uniformity, this would be a highly optimal case for minimizing temperature and densification nonuniformities. Overall, these results show that in the absence of scattering, heat transfer dynamics in a sample during UHS are influenced by $\bar{n}$ primarily via its effect on the surface reflectance and absorption coefficient, with different regimes separated by the $L = 3l$ condition.

The influence of scattering is made apparent through the results of Fig. 6. Higher scattering coefficients are observed to increase ΔT_{max}. Generally, a highly scattering medium will exhibit greater reflectance than an otherwise identical non-scattering medium due to enhanced diffuse reflectance from backscattering. As such, it may appear surprising that a higher diffuse reflectance results in a larger ΔT_{max} (Fig. 6a), while a higher Fresnel reflectance (higher n) results in a smaller ΔT_{max} (Fig. 5a). However, Fresnel reflectance occurs at the surface, while subsurface scattering is a volumetric phenomenon. Even with a large scattering coefficient, incident radiation which enters the medium and is subsequently backscattered still experiences attenuation as it travels through the volume. Therefore, a scattering medium with sufficient absorption not only preferentially absorbs at the surface, but also limits radiative penetration. This enhances resistance to radiative heat transfer through the medium, resulting in a larger ΔT_{max}.

The influence of σ_s on t_{ss} is dependent on whether the medium is highly absorbing ($3l \ll L$) or has low/intermediate absorbance ($3l \geq L$). In highly absorbing media, the medium reaches steady state slightly faster when scattering is increased. On the other hand, low/intermediately absorbing media take longer to reach steady state for higher scattering coefficients. These behaviors express a nuanced relationship between an increased path length and diffuse reflectance from scattering, a change in the distribution of absorbed intensity, and the interplay between conduction and radiation. We attribute the prolonged heating time in low absorption media to enhanced extinction and diffuse reflectance losses, and the more rapid heating in high absorption media to enhanced radiative diffusion from scattering. In the latter case, diffuse losses are unlikely to contribute as the absorption length is sufficiently small. While additional analyses may provide additional detail, t_{ss} varies only minimally with scattering, such that realistic optimization of UHS will not be hindered by this uncertainty.

In all cases, noticeable changes in ΔT_{max} and t_{ss} occur only once σ_s is of comparable magnitude to α. The scattering albedo ω represents the amount of scattering relative to total extinction, making it a useful metric to present absorption and scattering interplay more clearly. Figs. 6c–d present results in terms of variable ω rather than α and ω individually. Trends of ΔT_{max} are clearer from this perspective: temperature differences increase exponentially with scattering albedo, with the magnitude of ΔT_{max} being dictated by α. Looking back at Fig. 2, it is worth noting the similarities in the response of ΔT_{max} to reductions in k (higher conductive resistance) and increases in ω (higher radiative resistance). In contrast, behaviors remain difficult to generalize for t_{ss}. These results show that ΔT_{max} is clearly proportional to scattering albedo, while t_{ss} has a less sensitive and varied response to changes in scattering.

Finally, a simultaneous parametrization of thermal and optical properties is shown in Fig. 7. Here, absorption coefficient, scattering albedo, and thermal conductivity are varied, resulting in hierarchical trends. The inversely proportional and exponential dependence of ΔT_{max} on k is similar to that of Fig. 2a, and additional scattering continues to increase ΔT_{max} for all k. Lower absorption coefficients also reduce temperature differences for the same reasons discussed previously. For ΔT_{max}, these effects are additive, with all influencing the thermal response simultaneously. As for t_{ss}, multiple regimes are observed once again. In highly absorbing cases, t_{ss} decreases with higher D (as in Fig. 2d), but for lower absorption coefficients, the steady state time is dictated by absorption and independent of k. Scattering may also slightly lower or slightly raise t_{ss} depending on the absorption regime, as was observed in Fig. 6d.

To generalize these trends as in Figs. 2c–d, we seek combined terms to isolate the parameters of influence, beginning with the same quantities (L/k and $L^2/4D + L\rho c_p/2\sigma T_h^3$). As is clear from Figs. 5 and 6, the proportionality between the absorption coefficient and medium thickness strongly influences thermal response. We therefore define a proportionality function Ψ as $\Psi = 1 - e^{-p(\alpha+\sigma_s)L}$ to help elucidate optical and thermal interplay (p is a dimensionless fitting parameter). This function captures the exponential dependence of intensity on absorption, scattering and path length, with a form similar to many fundamental equations which describe the extinction of light as it propagates through a medium [18]. Based on the relative magnitudes of L, α, and σ_s, Ψ incorporates the differences in thermal transport observed in different optical property regimes (e.g., low versus high extinction).

Figs. 7c–d present the simulation data of Fig. 7a–b plotted versus $L/k \cdot \Psi$ and $[L^2/4D + L\rho c_p/2\sigma T_h^3] \cdot \Psi$ to condense thermal and optical

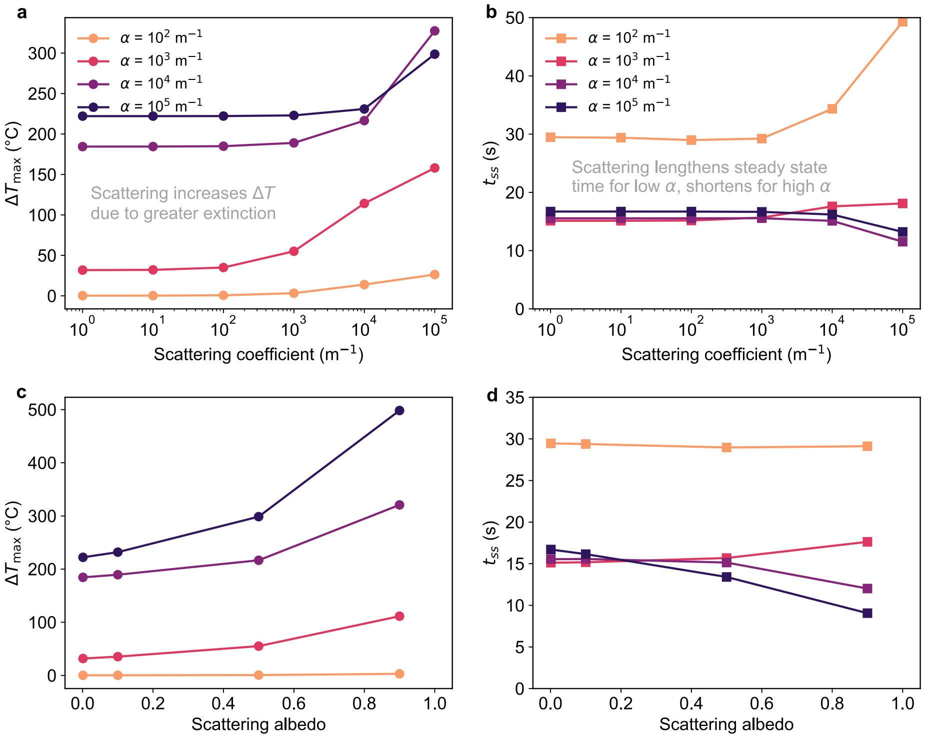

Fig. 6. Combined effects of scattering and absorption. Influence of scattering coefficient and absorption coefficient on (a) maximum temperature difference and (b) steady state time. Similar cases are shown in (c) and (d), respectively, but with variations in scattering albedo rather than scattering coefficient.

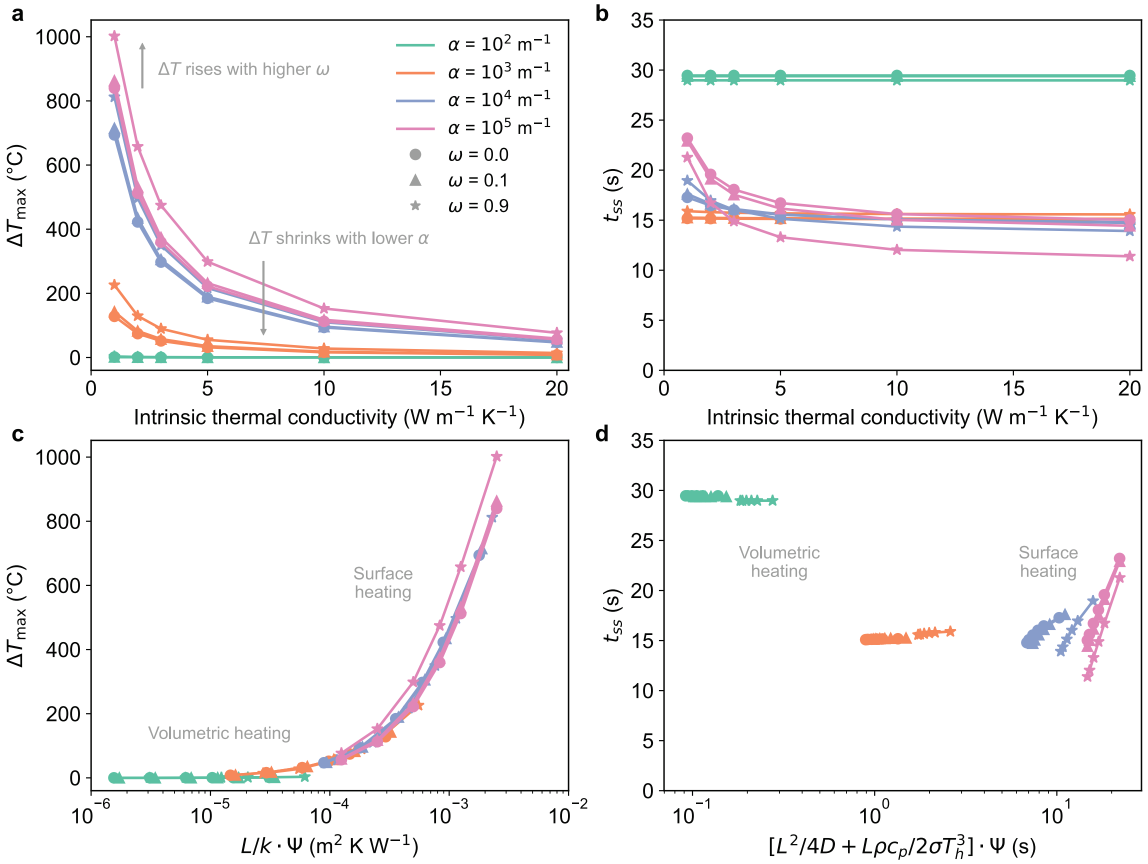

Fig. 7. Combined effects of thermal and optical properties on UHS thermal response. (a) Maximum temperature differences and (b) steady state times for selected variations in thermal conductivity, absorption coefficient, and scattering albedo. (c) and (d) show the same data plotted against modified scaling parameters to generalize the observed relationships. While ΔT_{max} shows a clear trend with the modified parameter, t_{ss} does not. A heater temperature of 1700 °C is used.

trends observed during UHS (note that these are the original forms of the scaling parameters from Fig. 2, to make clear that T_h and t_r are not explicitly varied in these parameterizations). A value of 0.05 is found to be suitable for p. A very reasonable trend of $\Delta T_{\max}$ with $L/k \cdot \Psi$ is obtained, as seen in Fig. 7c. Some separation of curves is observed for highly scattering cases; however, considering the complexity of the simulated cases, $L/k \cdot \Psi$ is quite capable of generalizing trends of $\Delta T_{\max}$ for vastly different sets of thermal and optical properties. For t_{ss}, though, optical properties continue to complicate trends due to several reasons. First, Ψ is a monotonic function, whereas t_{ss} exhibits non-monotonic behaviors with optical properties (for example, having local maxima at both very low and very high values of the absorption coefficient). Additionally, the derivation of $[L^2/4D + L\rho c_p/2\sigma T_h^3]$ assumes radiative absorption and thermal diffusion occur in series. While this is applicable to earlier highly absorbing cases, this assumption breaks down as absorption coefficients decrease and energy transport by conduction and radiation become more independent of one another. While a more in-depth and focused analysis on t_{ss} may reveal a clearer trend, this quantity varies only about 2× across these parameters. As this level of variation in the heating time scale is unlikely to hinder practical UHS process design, this approach may be used to obtain an order-of-magnitude estimate for t_{ss}.

3.3. Temperature dependence and densification

Until this point, simulations have assumed a constant relative density of 0.6, representative of a powder compact in the earliest stages of sintering. In practice, density will evolve during UHS – often quite rapidly – which can have pronounced effects on temperatures (and densities themselves, due to nonlinearities). Additionally, thermal and optical properties may be functions of temperature, density, or both, changing quickly as the material heats and sinters. In this section, we present results for two systems – alumina and yttria-stabilized zirconia (YSZ) – considering both temperature dependence and densification. These materials are used for illustration as both have relatively low thermal conductivities, and MSC data exists for high purity, sub-micron powders.

Four simulation cases are considered for the same heating parameters: with and without densification, and with and without thermal property temperature dependence. Literature MSCs and thermal property data are used for alumina [23,35] and YSZ [36–38]. For the non-densifying cases, the lowest point on the MSC (the green relative density) is used as a constant relative density. Optical constant data is obtained from ellipsometer measurements for alumina, and is taken from the literature for YSZ [39]. For cases that do not consider temperature dependence, properties are evaluated halfway between the ambient and sintering temperatures (e.g., for the employed sintering temperature of 1650 °C, k and c_p are evaluated at 815 °C and treated as constants). We assume a starting particle diameter of 200 nm (corresponding to many high-quality industrial ceramic powders [33]). Inputs for these simulations are summarized in Table S1.

These results are shown in Figs. 8–9 and S5–S7. For both materials, ΔT spikes in the early stages of the simulation, followed by a gradual approach to steady state within the first 30 s. For alumina, two distinct behaviors are observed for different models. For constant property models, $\Delta T_{\max}$ is slightly higher and occurs earlier than for temperature dependent models. As in many ceramics, the thermal conductivity of alumina is inversely proportional with temperature from ambient to high temperatures (up until a minimum value of k is reached). Therefore, choosing a constant k at an intermediate temperature is an underprediction in the first few seconds (k_{alumina}, for example, drops from about 33 to 7.5 W m^{-1} K^{-1} as it rises from room temperature to 850 °C). Thus, $\Delta T_{\max}$ occurs slightly earlier and with greater magnitude than in the temperature dependent cases. This is a shared characteristic for YSZ, and occurs regardless of whether densification is modeled.

Secondly, considering densification lowers t_{ss}. Both alumina and YSZ experience substantial densification prior to reaching steady state in these simulations. As per our model, densification raises k, lowers L, and results in more efficient absorption and less scattering. According to previous analyses, these factors lead to enhanced thermal dissipation and accelerate equilibration. This is obvious from Figs. 8a and 9a, where ΔT curves for densifying cases decrease more rapidly around 5–7.5 s — approximately when the materials begin densifying. Note also that YSZ experiences far greater temperature nonuniformity than alumina. This is because the thermal conductivity of YSZ is about 3 times lower, while its absorption coefficient is roughly the same as that of alumina in this wavelength region. With these characteristics, YSZ is an example of a material that would particularly benefit from model-informed UHS process design.

Assuming constant properties and neglecting densification results in overpredictions in $\Delta T_{\max}$ and t_{ss}, but the magnitudes of these deviations are not overly severe. Simulating temperature dependence and densification will provide higher accuracy, but deviations when these factors are neglected are within 10%–20%. The major utility of this model is to estimate sintering homogeneity and temperature rise time scales within samples during UHS. While a simulation fully integrated with temperature dependent properties and MSC data will provide a more precise estimate, even a simplified case offers insights with reasonable accuracy which can be used to improve UHS parameter design. It is also worth commenting on the interplay between densification and thermal response. Densification results in more rapid temperature stabilization, but does not influence $\Delta T_{\max}$, as the largest temperature difference occurs prior to the onset of densification in these cases.

Simulated differences of ρ_{rel} are also worth discussing: in these simulations, large inhomogeneities in temperature cause differences in sintering activity between the surface and center regions, with the surface densifying quicker than the inside. However, when the simulated density distribution is nonuniform, it may not be identical to that of a physical system. The MSC approach assumes that samples experience uniform heating, which is not true in such cases. Furthermore, preferential densification at sample surfaces may cause constrained sintering, introducing stresses that prevent other regions from densifying. As our model does not incorporate mechanics nor explicitly adapt the MSC to nonuniform heating, spatial distributions of ρ_{rel} in cases with low sintering uniformity may likely deviate from experiments. However, the magnitude and temporal distribution of $\Delta\rho_{\text{rel}}$ remains a valuable metric for assessing sintering uniformity and designing UHS procedures. Without considering densification, dense and uniform UHS samples may be sought by optimizing for minimal $\Delta T_{\max}$ and t_{ss} simultaneously. Yet, the densification dynamics of different materials have different dependencies on temperature. Thus, by incorporating MSC data, one may optimize for minimal $\Delta\rho_{\text{rel}}$ and time to full densification, thereby incorporating the detailed temperature dynamics of densification for a specific material.

4. Experimental validation

To validate the model, alumina (AKP-50, Sumitomo Chemical Co.) powder compacts are sintered using UHS, and densities are compared with model predictions (Fig. 10). Seven different sintering procedures are performed to yield a range of densities as outlined in Table 1. During each experiment, time-dependent heater temperatures are recorded. These temperatures are then used as the heater temperature within the simulation (considering both property temperature dependence and densification) as shown in Fig. 10b. The average density calculated by the model after heating is then compared with experimental measurements of density, as shown in Fig. 10c. Additional details on the experimental procedures are provided in the experimental methods section.

Good agreement between experimental and model-predicted densities is obtained across a range of sintered densities, from close to the

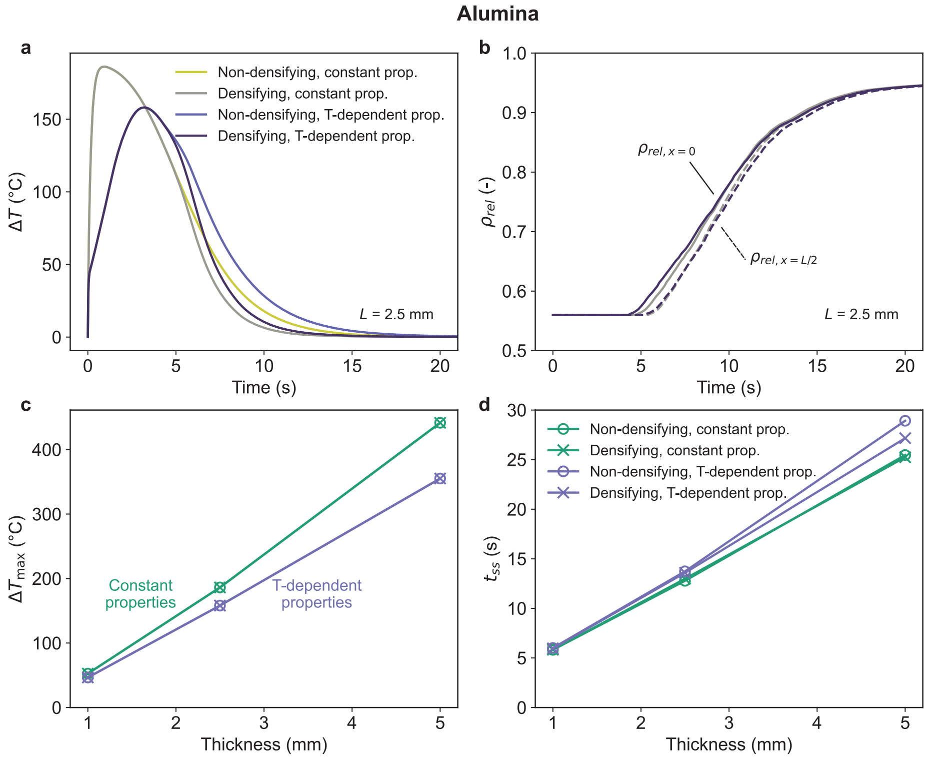

Fig. 8. Influence of densification and temperature dependence of alumina on simulation results. (a) Temperature differences versus time for a 2.5 mm thick alumina medium sintered at 1650 °C, simulated using different densification and temperature dependence assumptions. Corresponding evolutions in relative density for densifying cases are shown in (b). (c) and (d) provide comparative results when different assumptions are used for maximum temperature difference and steady state time.

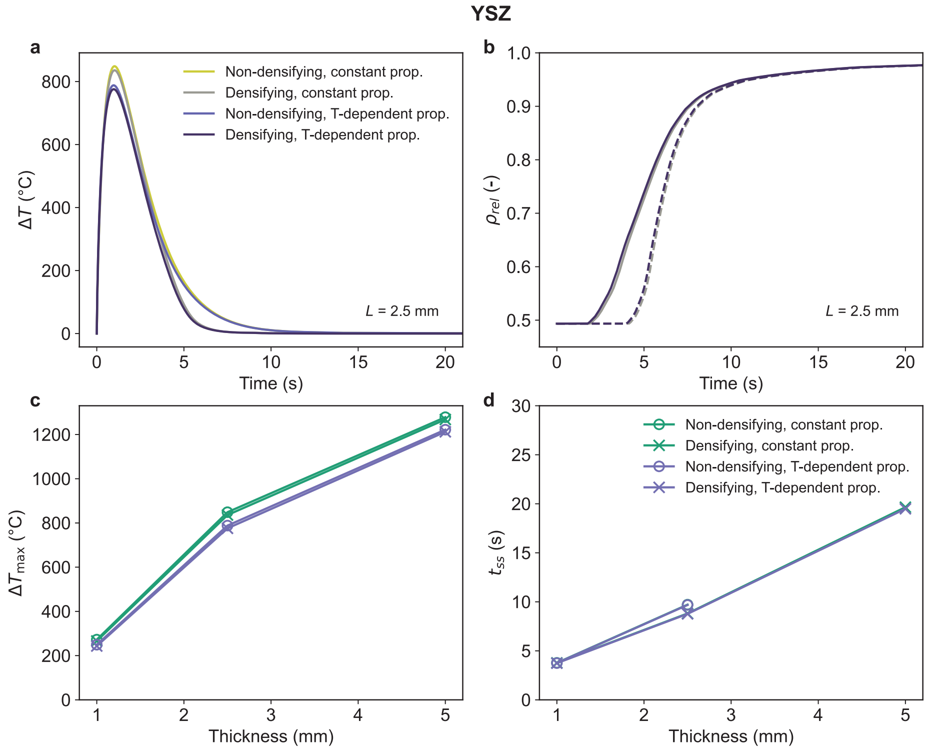

Fig. 9. Influence of densification and temperature dependence of YSZ on simulation results. (a) Temperature differences versus time for a 2.5 mm thick YSZ medium sintered at 1650 °C, simulated using different densification and temperature dependence assumptions. Corresponding evolutions in relative density for densifying cases are shown in (b). (c) and (d) provide comparative results when different assumptions are used for maximum temperature difference and steady state time.

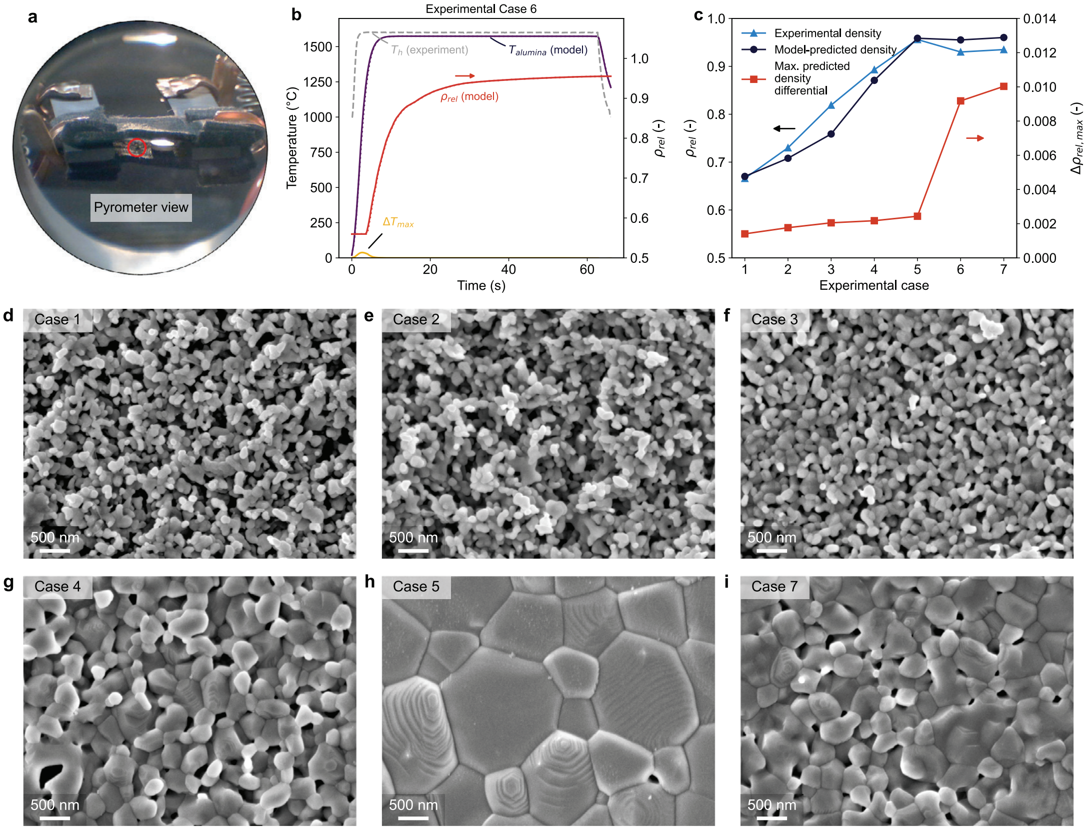

Fig. 10. Experimental validation. (a) Pyrometer view of UHS heating elements. Due to slight spatial variations in temperature along the length of each felt, pressed powder samples are placed slightly off-center, while the pyrometer measures the corresponding location in the other direction to provide a more reliable temperature measurement. (b) Simulation results obtained using measured heater temperatures as model inputs, illustrated for Case 6. Simulated temperature and relative density curves are shown, with solid and dashed lines for top and bottom surface temperatures, respectively. The final density estimated by the model is the average density within the medium after the final time step. Note that the maximum sample temperature is slightly below the heater temperature as the emittance of the heater is less than 1.0, as determined experimentally. (c) Comparison of measured and predicted relative densities for different experimental cases. Case parameters are given in Table 1. The maximum difference in relative density predicted for each case is also shown on the right y-axis. (d–i) SEM micrographs of sintered alumina at magnifications of approximately 20 kx. Images are taken on the bottom face of all samples for consistency. Additional SEM images are provided in Figs. S9 and S10.

Table 1
UHS parameters for alumina sintering experiments shown in Fig. 10. A heating rate of ~1000 °C s^{-1} indicates the heater was brought to temperature as rapidly as possible (within 1–2 s).

Experimental case	Hold temperature (°C)	Heating rate (°C s^{-1})	Hold time (s)
1	1350	23	60
2	1375	23	35
3	1400	23	55
4	1500	23	35
5	1600	23	75
6	1600	~1000	60
7	1600	~1000	90

green density to near-theoretical density. The largest deviation (about 7%) in predictions occurs around 75% relative density, where the MSC slope is steepest. As a result, density predictions are most susceptible to small errors in this range. Otherwise, model-predicted densities are within 3% of the experimental measurements. These results illustrate that the constructed simulation model produces accurate results for temperature and densification during UHS.

Samples are imaged using SEM to validate density measurements and draw further conclusions from the microstructure. Figs. 10d–i and S9–S10 show that microstructures are consistent with experimentally measured densities. The first two cases show little densification with only early-stage neck growth. As sintering temperatures increase and longer times are used, neck growth continues and initial grains begin to form (Cases 3 and 4). Case 5 illustrates a very dense structure with larger grains, though the grains themselves are still reasonably small (about 1 μm or less).

Of particular note are differences in the densities and microstructures of Cases 5–7. Using our model, these cases were designed to sinter alumina to near-theoretical density, as demonstrated by the simulation predictions in Fig. 10c. However, Case 5 achieves a higher density than 6 and 7, despite nearly identical values of predicted density and sintering function Θ (Fig. S8). The key distinction is the heating rate: Case 5 ramps the heater to 1600 °C over 60 s (23 °C s^{-1}), while Cases 6 and 7 ramp the heater as quickly as possible (1–2 s). Compared with Case 5, the near-instantaneous heater temperature rise used in Cases 6 and 7 results in larger differences of ρ_{rel} and temperature (shown in Figs. 10c and S8), indicating a high sintering nonuniformity. As such, the more rapidly heated samples may experience constrained sintering and limited densification. The SEM images for Cases 6 and 7 depict a less dense microstructure than that of Case 5 (Figs. 10, S9 and S10), agreeing with the density measurements. Furthermore, Cases 6 and 7 have similar experimentally-measured densities and porous microstructures despite Case 7 being sintered 50% longer. In sum, large model-predicted temperature and density inhomogeneities correspond to lower densities, and extending sintering time does not aid densification when the heating rate is very rapid. This indicates that temperature uniformity-related issues constrain densification and lead to departures from MSC predictions, and that our model provides a measure of these behaviors. Thus, this model is capable of optimizing

UHS processes to produce highly dense and uniform materials, which can be performed by minimizing simulated temperature and density differences.

5. Discussion

This UHS simulation model is useful as both a general tool to establish thermal trends in materials of different properties, and as a highly detailed tool through which UHS procedures may be designed to optimize uniformity when sintering specific materials. For highly absorbing media, maximum temperature differences are dictated by the conductive resistance, heater temperature, and dimensionless ramp time ($(L/k)T_h^4 Fo_{t_r}^{-1}$), and heating times trend with thermal mass, conductive and radiative resistance, and the ramp time ($[L^2/4D + L\rho c_p/2\sigma T_h^3 + (T_h \cdot 10^{-4} + 0.61)t_r]$). Equations for estimating temperature differences and heating times based on these relationships are provided in Fig. 4. Higher sintering temperatures cause more rapid heating and larger temperature differences, and temperature differences may be reduced by slowing the heating rate at the expense of heating time. Thermal response is highly dependent on the absorption coefficient, with a transition between volumetric and surface heating at $3l = L$. When the absorption length is comparable to the medium thickness, an optimal balance between heating time and temperature difference is obtained. Additionally, optical scattering is found to increase temperature difference due to increased resistance to radiative transfer. Overall, we find that both the thermal and optical property trends influence thermal response simultaneously, with k/L and α/L emerging as the most important dictating material properties for heating uniformity. The dependence of the thermal response on absorption and scattering, in particular when materials are not both highly absorbing and non-scattering, highlights the necessity of considering radiative transport within the medium during UHS. When the property temperature dependence and density evolutions are considered, the same trends are generally observed. Considering that densification causes steady state to be achieved slightly more rapidly, selecting a constant k at an intermediate temperature (rather than considering temperature dependence) results in a minor over-prediction of $\Delta T_{\max}$. Even so, good estimates for temperature homogeneity and steady-state time scales can still be achieved without incorporating densification and temperature dependence.

Experimentally, we find that density predictions are more accurate when spatial differences in density and temperature are low. In our demonstration with alumina, departures from density predictions and signs of constrained sintering appear for relative density and temperature differences of 1% and 40 °C, respectively. Less rapid heating rates reduce these differences to 0.2% and 5 °C and produce higher-density samples. This also validates the earlier supposition that sintering nonuniformity may be reduced by extending the ramp time. The threshold of temperature or density uniformity at which densification becomes constrained may vary with material choice and particle morphology due to differences in sintering activity. However, choosing heating schedules that limit temperature differences to several degrees Celsius and density differences to about a tenth of a percent (which may be done through this model) appears an appropriate starting point. While performing such optimizations with MSC data and temperature-dependent properties is most accurate, optimizing for temperature uniformity with constant properties presents a less complex alternative. The latter approach provides more conservative results, as it neglects the material-specific temperature dependencies of properties and sintering which tends to result in slight overestimates of $\Delta T_{\max}$ and t_{ss}. Nonetheless, both approaches offer good opportunities for researchers to optimize UHS procedures for diverse materials without engaging in time-intensive experimental trial and error.

It is worth emphasizing the limitations of this methodology and areas for future work. One shortcoming of the 1D model developed in this work is that it does not incorporate the effects of stress gradients that arise due to mechanical constraints from regions that densify more quickly. This would require a two- or three-dimensional model that also couples long-range densification stresses and stress relaxation mechanisms, such as creep, as a function of temperature and density. This would greatly complicate the model, and for this reason, we have adopted $\Delta T_{\max}$ as a proxy for densification differences. It is likely, though, that as the densification during UHS is so rapid, stress relaxation is unlikely to occur. Also, although the focus of this contribution has been on low thermal conductivity materials, the same model applies to the sintering of metals and alloy powders. However, their significantly higher thermal conductivity will prevent a large $\Delta T_{\max}$ from developing during UHS and, consequently, lower the likelihood of density gradients and constrained sintering. In addition, we have illustrated accuracy for relatively thin samples which may be approximated as 1D domains; however, geometries which deviate from this will require expansion into 2D or 3D coordinate systems. Also, extending the MSC approach to materials of different grain size or composition requires identifying (or generating) suitable empirical data to construct an MSC, which may be labor-intensive if it does not already exist. Finally, more detailed factors such as grain size and morphology evolution, scattering anisotropy, and the magnitude of surface conduction and convection effects may be considered as well. These limitations present opportunities for future work in similar areas.

6. Conclusion

We have developed a Python-based simulation model for heat transfer and densification in powder compacts densified by UHS. The model combines the influences of thermal and optical properties to accurately assess temperature and densification uniformity in materials, considering property dependencies on temperature, density, particle size, and spectral variation. Using this model, we find that sintering uniformity is most dependent on the thermal conductivity, absorption coefficient, and thickness of the material. In particular, the relative absorption depth of the material determines whether heating is concentrated at the surface or distributed volumetrically, which has a large influence on uniformity. Good agreement between experimental and modeled densities is observed, which validates model accuracy. We show that minimizing simulated temperature and density differences produces denser, more uniform samples, illustrating the utility of this model for informing rapid sintering process design. We also provide a new method for estimating temperature uniformity and heating time scales for a variety of materials, geometries, and sintering parameters. These findings and the simulation model may be used as a reference to design UHS procedures that produce uniformly sintered samples for diverse materials, circumventing time-consuming experimentation.

Experimental methods

For experimental sintering demonstrations, high-purity alumina was obtained from Sumitomo Chemical Co. (AKP-50, purity ≥ 99.99%, D50 200 nm). Powder compacts are produced by adding 0.17 g of alumina to a 10 mm diameter cylindrical die. The powder is pressed at 2 MT using a Carver hydraulic press for 3 min, after which they are transferred to the UHS system for sintering.

The UHS system is housed in a vacuum chamber (see Fig. S3). The chamber is pumped to 300 mTorr and subsequently filled with argon gas prior to sintering. A power supply (Elektro-Automatik, 100080-170) provides the electrical power input. Carbon felt (Fuel Cell Store, 3.1 mm Rayon Carbon Felt, 22070012) is used for the heating elements. Two identical pieces of felt are cut into dog bone shapes, with the center section being 30 × 25 mm and both ends being 20 × 30 mm. The felts are then sandwiched around graphite blocks, which are attached to the power supply using high-current alligator clips. Green powder compacts are placed between the two felts for sintering. A vertical spacing of about 8 mm is maintained between the two felts to facilitate accurate temperature measurement. A two-color pyrometer (Optris CSvision R1M) is used to measure the inside surface temperature of the bottom felt (the inside surface must be used for measurement as the outside surface may be several hundred degrees Celsius cooler than the inside). The felts also display minor lateral temperature deviations (about 10–30 °C), with the center of the felt being the hottest. To measure the temperature that the sample experiences most accurately, the powder compact is positioned slightly off-center such that the pyrometer can measure the corresponding off-center location in the other direction. Temperatures are set and controlled via PID using a custom built LabVIEW VI, which modifies voltage to achieve user-specified temperatures and heating rates. After sintering, density is measured according to ASTM C373.

For the modeling of experimental cases, the emittance of the carbon felt heating elements is determined from hemispherical reflectance and transmittance measurements. From 0.35–2.5 μm, a Hitachi U-4100 spectrometer with an integrating sphere is used. From 2.5–20 μm, a ThermoFisher Nicolet iS50 FTIR spectrometer with a PIKE DiffusIR integrating sphere is used. The emittance of the felt is determined based on a Planck average of emittance using the maximum temperature of the heater as the emission temperature. The determined emittance value is approximately 0.95 for all experimental cases. SEM images are obtained using a Zeiss Gemini 360 FE-SEM at an acceleration voltage of 5 kV. Samples are sputter coated with 10 nm of Pt/Pd prior to imaging. Optical constants for alumina are obtained from a polycrystalline sapphire wafer (Saint-Gobain) using a JA Woollam IR-VASE Mk 2 spectroscopic ellipsometer.

Declaration of competing interest

The authors declare that they have no known competing financial interests or personal relationships that could have appeared to influence the work reported in this paper.

Acknowledgments

The authors are grateful to Prof. Patrick E. Hopkins and Dr. Saman Zare for providing optical constant data for alumina, and Katelyn Miller for her assistance in the preparation of alumina samples. This work is supported by the Advanced Research Projects Agency-Energy (ARPA-E), USA through grant number DE-AR0001809.

Appendix A. Supplementary data

Supplementary material related to this article can be found online at https://doi.org/10.1016/j.applthermaleng.2026.131403.

Data availability

Data will be made available on request.

References

[1] W.D. Kingery, H.K. Bowen, D.R. Uhlmann, Introduction to Ceramics, John Wiley & Sons, 1976.

[2] Y.M. Chiang, D. Birnie, W.D. Kingery, Physical Ceramics: Principles for Ceramic Science and Engineering, John Wiley & Sons, 1997.

[3] M. Ashby, A first report on sintering diagrams, Acta Metall. 22 (3) (1974) 275–289.

[4] B.C. Wyatt, S.K. Nemani, G.E. Hilmas, E.J. Opila, B. Anasori, Ultra-high temperature ceramics for extreme environments, Nat. Rev. Mater. 9 (11) (2024) 773–789, http://dx.doi.org/10.1038/s41578-023-00619-0.

[5] L. Dejonghe, M. Rahaman, Handbook of Advanced Ceramics, vol. I, Elsevier, 2003, pp. 187–264, http://dx.doi.org/10.1016/B978-012654640-8/50006-7.

[6] X. Kuang, G. Carotenuto, L. Nicolais, A review of ceramic sintering and suggestions on reducing sintering temperatures, Adv. Perform. Mater. 4 (3) (1997) 257–274, http://dx.doi.org/10.1023/A:1008621020555.

[7] L. Karacasulu, C. Manière, C. Vakifahmetoglu, S. Marinel, M. Biesuz, Sintering under high heating rates, Annu. Rev. Mater. Res. 55 (2025) 203–230, http://dx.doi.org/10.1146/annurev-matsci-080323-042441, (Volume 55, 2025).

[8] I.W. Chen, X.H. Wang, Sintering dense nanocrystalline ceramics without final-stage grain growth, Nature 404 (6774) (2000) 168–171, http://dx.doi.org/10.1038/35004548.

[9] C. Wang, W. Ping, Q. Bai, H. Cui, R. Hensleigh, R. Wang, A.H. Brozena, Z. Xu, J. Dai, Y. Pei, C. Zheng, G. Pastel, J. Gao, X. Wang, H. Wang, J.C. Zhao, B. Yang, X.R. Zheng, J. Luo, Y. Mo, B. Dunn, L. Hu, A general method to synthesize and sinter bulk ceramics in seconds, Science 368 (6490) (2020) 521–526, http://dx.doi.org/10.1126/science.aaz7681.

[10] M. Kermani, C. Hu, S. Grasso, From pit fire to Ultrafast High-temperature Sintering (UHS): A review on ultrarapid consolidation, Ceram. Int. 49 (3) (2023) 4017–4029, http://dx.doi.org/10.1016/j.ceramint.2022.11.091.

[11] M.A. Janney, C.L. Calhoun, H.D. Kimrey, Microwave sintering of solid oxide fuel cell materials: I, Zirconia-8 mol% Yttria, J. Am. Ceram. Soc. 75 (2) (1992) 341–346, http://dx.doi.org/10.1111/j.1151-2916.1992.tb08184.x.

[12] P. Cavaliere, B. Sadeghi, A. Shabani, in: P. Cavaliere (Ed.), Spark Plasma Sintering of Materials: Advances in Processing and Applications, Springer International Publishing, Cham, 2019, pp. 3–20, http://dx.doi.org/10.1007/978-3-030-05327-7_1.

[13] Z. Lin, X. Zhao, C. Wang, Q. Dong, J. Qian, G. Zhang, A.H. Brozena, X. Wang, S. He, W. Ping, G. Chen, Y. Pei, C. Zheng, B.C. Clifford, M. Hong, Y. Wu, B. Yang, J. Luo, P. Albertus, L. Hu, Rapid pressureless sintering of glasses, Small 18 (17) (2022) 2107951, http://dx.doi.org/10.1002/smll.202107951.

[14] C. Wang, W. Zhong, W. Ping, Z. Lin, R. Wang, J. Dai, M. Guo, W. Xiong, J.C. Zhao, L. Hu, Rapid synthesis and sintering of metals from powders, Adv. Sci. 8 (12) (2021) 2004229, http://dx.doi.org/10.1002/advs.202004229.

[15] H. Xie, V.K. Champagne III, W. Zhong, B. Clifford, S. Liu, L. Hu, J.C. Zhao, D.R. Clarke, Design, fabrication, and screening of environmental-thermal barrier coatings prepared by ultrafast high-temperature sintering, Adv. Funct. Mater. 34 (10) (2024) 2309978, http://dx.doi.org/10.1002/adfm.202309978.

[16] M. Guo, Q. Dong, H. Xie, C. Wang, Y. Zhao, X. Wang, W. Zhong, Z. Li, R. Wang, Y. Wang, L. Hao, S. He, G. Chen, W. Xiong, J.C. Zhao, L. Hu, Ultrafast high-temperature sintering to avoid metal loss toward high-performance and scalable cermets, Matter 5 (2) (2022) 594–604, http://dx.doi.org/10.1016/j.matt.2021.11.008.

[17] Z. Guo, R.I. Todd, Acceleration of grain boundary diffusion during ultra-fast firing (UHS) of alumina powder compacts, Acta Mater. 282 (2025) 120471, http://dx.doi.org/10.1016/j.actamat.2024.120471.

[18] M.F. Modest, Radiative Heat Transfer, third ed., Academic Press, New York, 2013.

[19] D. Green, O. Guillon, J. Rödel, Constrained sintering: A delicate balance of scales, J. Eur. Ceram. Soc. 28 (2008) 1451–1466, http://dx.doi.org/10.1016/j.jeurceramsoc.2007.12.012.

[20] S.E. Schoenberg, D.J. Green, A.E. Segall, G.L. Messing, A.S. Grader, P.M. Halleck, Stresses and distortion due to green density gradients during densification, J. Am. Ceram. Soc. 89 (10) (2006) 3027–3033, http://dx.doi.org/10.1111/j.1551-2916.2006.01182.x.

[21] S.J. Bennison, M.P. Harmer, Effect of MgO solute on the kinetics of grain growth in A12O3, J. Am. Ceram. Soc. 66 (5) (1983) C–90–C–92, http://dx.doi.org/10.1111/j.1151-2916.1983.tb10065.x.

[22] N. Shaw, R. Brook, Structure and grain coarsening during the sintering of alumina, J. Am. Ceram. Soc. 69 (2) (1986) 107–110, http://dx.doi.org/10.1111/j.1151-2916.1986.tb04711.x.

[23] H. Su, D.L. Johnson, Master sintering curve: A practical approach to sintering, J. Am. Ceram. Soc. 79 (12) (1996) 3211–3217, http://dx.doi.org/10.1111/j.1151-2916.1996.tb08097.x.

[24] DeWitt Incropera, Bergman, Lavine, Fundamentals of Heat and Mass Transfer, Sixth ed., John Wiley & Sons, 2006.

[25] R. Siegel, J. Howell, Thermal Radiation Heat Transfer, fourth ed., Taylor & Francis, 2002.

[26] D.S. McLachlan, M. Blaszkiewicz, R.E. Newnham, Electrical resistivity of composites, J. Am. Ceram. Soc. 73 (8) (1990) 2187–2203, http://dx.doi.org/10.1111/j.1151-2916.1990.tb07576.x.

[27] C.W. Nan, R. Birringer, D.R. Clarke, H. Gleiter, Effective thermal conductivity of particulate composites with interfacial thermal resistance, J. Appl. Phys. 81 (10) (1997) 6692–6699, http://dx.doi.org/10.1063/1.365209.

[28] W. Pabst, E. Gregorová, A new percolation-threshold relation for the porosity dependence of thermal conductivity, Ceram. Int. 32 (1) (2006) 89–91, http://dx.doi.org/10.1016/j.ceramint.2004.12.007.

[29] W. Pabst, E. Gregorová, Critical Assessment 18: Elastic and thermal properties of porous materials – rigorous bounds and cross-property relations, Mater. Sci. Technol. 31 (15) (2015) 1801–1808, http://dx.doi.org/10.1080/02670836.2015.1114697.

[30] C.H. Lange, D.D. Duncan, Temperature Coefficients of the Refractive Index for Candidate Optical Windows, Johns Hopkins APL Technical Digest, 1993.

[31] S. Prahl, Miepython: A Python library for Mie scattering calculations, 2025, http://dx.doi.org/10.5281/zenodo.7949263, URL https://github.com/scottprahl/miepython.

[32] S.M. Sweeney, M.J. Mayo, Relation of pore size to green density: The Kozeny Equation, J. Am. Ceram. Soc. 82 (7) (1999) 1931–1933, http://dx.doi.org/10.1111/j.1151-2916.1999.tb02020.x.

[33] P.L. Chen, I.W. Chen, Sintering of fine oxide powders: I, microstructural evolution, J. Am. Ceram. Soc. 79 (12) (1996) 3129–3141, http://dx.doi.org/10.1111/j.1151-2916.1996.tb08087.x.

[34] J.A. Varela, O.J. Whittemore, E. Longo, Pore size evolution during sintering of ceramic oxides, Ceram. Int. 16 (3) (1990) 177–189, http://dx.doi.org/10.1016/0272-8842(90)90053-I.

[35] R.G. Munro, Evaluated material properties for a sintered alpha-alumina, J. Am. Ceram. Soc. 80 (8) (1997) 1919–1928, http://dx.doi.org/10.1111/j.1151-2916.1997.tb03074.x.

[36] M. Biesuz, E. De Bona, C. Manière, Fast firing of 3 mol% yttria-stabilized zirconia: On the effect of heating rate on sintering, J. Am. Ceram. Soc. 107 (10) (2024) 6596–6606, http://dx.doi.org/10.1111/jace.19989.

[37] D.R. Clarke, S.R. Phillpot, Thermal barrier coating materials, Mater. Today 8 (6) (2005) 22–29, http://dx.doi.org/10.1016/S1369-7021(05)70934-2.

[38] M. Radovic, E. Lara-Curzio, R.M. Trejo, H. Wang, W.D. Porter, Advances in Solid Oxide Fuel Cells II: Ceramic Engineering and Science Proceedings, John Wiley & Sons Ltd, 2006, pp. 79–85, http://dx.doi.org/10.1002/9780470291337.ch8.

[39] J.A. Nychka, M.R. Winter, D.R. Clarke, T. Naganuma, Y. Kagawa, Temperature-dependent optical reflectivity of Tetragonal-Prime Yttria-Stabilized Zirconia, J. Am. Ceram. Soc. 89 (3) (2006) 908–913, http://dx.doi.org/10.1111/j.1551-2916.2005.00813.x.